

Rethinking RSSI for WiFi Sensing

Zhongqin Wang^{1,2*}, J. Andrew Zhang^{1,2*}, Kai Wu^{1,2} and Y. Jay Guo^{1,2}

¹School of Electrical and Data Engineering, University of Technology Sydney, Sydney, NSW, 2007, Australia.

²Global Big Data Technologies Centre, University of Technology Sydney, Sydney, NSW, 2007, Australia.

*Corresponding author(s). E-mail(s): zhongqin.wang@uts.edu.au; andrew.zhang@uts.edu.au;
Contributing authors: kai.wu@uts.edu.au; jay.guo@uts.edu.au;

Abstract

The Received Signal Strength Indicator (RSSI) is widely available on commodity WiFi devices but is commonly regarded as too coarse for fine-grained sensing. This paper revisits its sensing potential and presents *WiRSSI*, a bistatic WiFi sensing framework for passive human tracking using only RSSI measurements. WiRSSI adopts a 1Tx-3Rx configuration and is readily extensible to Multiple-Input Multiple-Output (MIMO) deployments. We first reveal how CSI power implicitly encodes phase-related information and how this relationship carries over to RSSI, showing that RSSI preserves exploitable Doppler, Angle-of-Arrival (AoA), and delay cues associated with human motion. WiRSSI then extracts Doppler-AoA features via a 2D Fast Fourier Transform and infers delay from amplitude-only information in the absence of subcarrier-level phase. The estimated AoA and delay are then mapped to Cartesian coordinates and denoised to recover motion trajectories. Experiments in practical environments show that WiRSSI achieves median XY localization errors of 0.905 m, 0.784 m, and 0.785 m for elliptical, linear, and rectangular trajectories, respectively. In comparison, a representative CSI-based method attains median errors of 0.574 m, 0.599 m, and 0.514 m, corresponding to an average accuracy gap of 0.26 m. These results demonstrate that, despite its lower resolution, RSSI can support practical passive sensing and offers a low-cost alternative to CSI-based WiFi sensing.

1 Introduction

Integrated Sensing and Communication (ISAC) has emerged as a key paradigm for next-generation communication systems, aiming to integrate environmental sensing and data communication into a unified framework [1, 2]. By enabling wireless signals to simultaneously convey information and perceive the surrounding environment, ISAC opens new opportunities in diverse applications such as environment sensing [3–7], human-computer interaction [8–10], and healthcare monitoring [11, 12]. These applications demand low-cost, device-free, and easily deployable sensing solutions that can operate within existing communication infrastructure. At present, WiFi is particularly appealing for realizing ISAC, as the IEEE 802.11bf amendment [13] introduces Channel State Information (CSI)-based sensing functionality into WiFi systems. This development marks a significant milestone toward large-scale ISAC deployment on commercial devices.

Despite these advances, most existing WiFi sensing studies rely heavily on CSI, which is not always accessible on commodity hardware. In contrast, the Received Signal Strength Indicator (RSSI) is readily available on nearly all commercial WiFi devices but has long been regarded as inadequate for fine-grained sensing. This view mainly stems from RSSI's coarse representation of the wireless channel: it reports only aggregated received power over the entire bandwidth, typically quantized at low resolution (e.g., 8-10 bits, ~ 1 dB per level), thereby discarding multipath diversity and limiting sensitivity to small-scale fading and micro-motion. In addition, RSSI is strongly influenced by hardware-dependent factors such as automatic gain control, antenna polarization mismatch, and RF front-end variations, leading to inconsistent power scaling across time and devices. As a result, RSSI has been widely considered incapable of capturing meaningful environmental or human-motion dynamics, motivating

the community's strong preference for CSI-based sensing. However, *is RSSI truly as unsuitable for sensing as commonly believed?*

RSSI-based WiFi sensing has been extensively studied over the past decades [14, 15]. Early studies primarily rely on the classical path loss model [16, 17] to estimate the distance between the transmitter and receiver. While such models can roughly capture large-scale attenuation for the active transceiver link, they face significant challenges in localizing passive targets. Low-resolution RSSI reflects only the aggregated received power from all propagation paths, making it difficult to isolate reflections associated with the objects of interest. Some works explore RSSI-based fingerprinting methods [18–20], which construct a database of received signal patterns at known locations and perform localization by matching the RSSI measurements to the closest stored fingerprints. Although this technique can achieve meter-level accuracy in same environments, it relies heavily on site-specific calibration and dense prior data collection. The resulting performance often deteriorates significantly when environmental conditions change, or when the target moves in unseen regions. These limitations motivate a more principled investigation of how RSSI encodes spatial, temporal, and geometric information, beyond empirical mapping or data-driven matching.

In recent years, more research efforts have shifted toward CSI-based sensing, as CSI provides detailed amplitude and phase measurements across subcarriers. However, CSI-based sensing suffers from a critical limitation, i.e., *clock asynchrony*, which introduces random phase distortions due to timing offset (TO) and carrier frequency offset (CFO) between the transmitter and receiver in bistatic configurations. These random phases significantly degrade sensing accuracy. Many techniques [21] have been proposed to eliminate random phase offsets in bistatic sensing, including multi-antenna and single-antenna methods. (1) *Multi-antenna*. A typical approach is Cross-Antenna Cross-Correlation (CACC) [22], which leverages at least two receiving antennas to exploit identical clock-induced distortions and thereby remove TO and CFO while preserving the linear relationship among delay, Doppler, and Angle of Arrival (AoA). However, its conjugate operation introduces signal parameter symmetry, preventing reliable determination of target motion direction. WiDFS [23] and WiDFS 2.0 [24] extends this idea with Differential CACC (DCACC) using three receiving antennas to suppress the mirror ambiguity. Cross-Antenna Signal-Ratio (CASR) [11, 25] instead computes CSI ratios between antennas to cancel random phases and AGC variations. However, its inherently nonlinear formulation complicates the estimation of delay and AoA. (2) *Single-antenna*. Several signal-antenna approaches construct reference signals to remove random phases. SHARP [26] applies compressed sensing to reconstruct the reference signal, but at a high computational cost. Cross-Frequency Cross-Correlation (CFCC) [27] exploits subcarrier-domain correlation to mitigate CFO, but it limits accurate delay and AoA estimation. Linear regression-based methods [28] roughly remove TO by fitting phase trends across subcarriers, yet they degrade under practical multipath due to nonlinear phase distortions. Recently, Self-Referencing Cross-Correlation (SRCC) [10] demonstrates better performance among single-antenna techniques. It constructs an energy-adjusted CSI in the subcarrier domain that shares the same TO and CFO as the original CSI, enabling robust phase compensation for unambiguous parameter estimation with very low computational complexity. Moreover, SRCC inherently mitigates hardware-induced inter-antenna phase offsets, enabling calibration-free AoA estimation. Although IEEE 802.11bf standardizes CSI-based WiFi sensing, power-domain measurements such as RSSI remain widely available on commodity WiFi devices, and their sensing potential has yet to be fully explored. Moreover, sensing insights from RSSI can also be exploited to enhance CSI sensing, which remains unexplored.

In this work, we revisit the physical-layer modeling of RSSI and show that, with appropriate processing, RSSI can serve as an effective signal source for passive WiFi sensing. We present *WiRSSI*, a bistatic WiFi sensing framework that enables passive target tracking using only RSSI measurements. WiRSSI adopts a 1Tx-3Rx deployment with spatially separated transmitter and receiver, achieves joint AoA and delay estimation from power-domain signals, and supports robust and continuous target tracking. The framework is readily extensible to Multiple-Input Multiple-Output (MIMO) deployments. The main contributions of this work are summarized as follows:

1) Unlike conventional path-loss RSSI models, we derive an RSSI signal-power model from aggregated CSI power, showing that RSSI, as a subcarrier-integrated power representation, implicitly encodes phase-related motion information and captures the relationship among Doppler, AoA, and delay.

2) We design a low-complexity feature extraction method based on a 2D Fast Fourier Transform (FFT) to jointly estimate Doppler and AoA features from multi-antenna RSSI measurements. In the absence of subcarrier-level information, amplitude-only features are further exploited to estimate target delay. Based on these features, WiRSSI enables target localization and continuous tracking in dynamic scenarios.

3) We implement a 1Tx-3Rx bistatic WiFi system using Intel 5300 NICs, which provide per-antenna RSSI readings alongside CSI measurements. Experiments are conducted on elliptical, linear, and rectangular trajectories, achieving median XY errors of 0.905 m, 0.784 m, and 0.785 m, respectively. For comparison, a representative CSI-based sensing framework [10] achieves median XY errors of 0.574 m, 0.599 m, and 0.514 m. Despite this

accuracy gap, the experimental results demonstrate the potential of low-resolution RSSI for low-cost and widely deployable ISAC applications.

2 CSI and RSSI Signal Models

This section examines the physical-layer relationship between CSI and RSSI, and shows how RSSI can be approximately related to aggregated CSI power across subcarriers.

2.1 Bistatic CSI Model

In bistatic systems, the transmitter and receiver are spatially separated and operate without a shared clock. As a result, the measured CSI at the receiver suffers from random phase distortions on every CSI sample, including a TO τ_k^{TO} and a CFO ϕ_k^{CFO} . In addition, each receiving antenna experiences a hardware-induced phase offset ϕ_j^{PO} , initialized by the hardware in the receiving chain, such as phase-locked loop (PLL), local oscillator, and RF cables, which may vary across devices and power cycles. Moreover, the received signal undergoes AGC adjustment, represented by a time-varying amplitude factor α_k . The AGC dynamically scales the baseband signal amplitude according to the instantaneous received power to prevent ADC saturation and maintain a stable signal level for demodulation. Consequently, the measured CSI is subject to multiple impairments, including random phase shifts from clock asynchrony, hardware-dependent per-antenna phase offsets, and AGC-induced amplitude scaling, all of which jointly distort the observed channel response.

Within a short-time coherent processing interval (CPI) [1] (e.g., 0.1 seconds interval), the time-varying amplitude factor α_k can be assumed to be constant. And let $CSI_{i,j,k}$ denote the measured CSI at the i -th Rx antenna, the j -th subcarrier, and the k -th time, which is modeled as:

$$CSI_{i,j,k} = \alpha e^{-J(2\pi f_j \tau_k^{\text{TO}} + \phi_k^{\text{CFO}} + \phi_i^{\text{PO}})} (H_{i,j}^S + H_{i,j,k}^X), \quad (1)$$

where

$$\begin{cases} H_{i,j}^S = \sum_{l_1} \rho_{i,j}^S[l_1] e^{-J2\pi f_j \tau_i^S[l_1]}, \\ H_{i,j,k}^X = \sum_{l_2} \rho_{i,j,k}^X[l_2] e^{-J2\pi(f_j \tau_k^X[l_2] + f_k^D[l_2](k-1)\Delta t + \frac{(i-1)}{2} \sin \theta_k^X[l_2])}. \end{cases} \quad (2)$$

Here, $H_{i,j}^S$ denotes the channel frequency response (CFR) of static paths, including Line-of-Sight (LOS), Non-Line-of-Sight (NLOS), and reflections from stationary objects such as walls, floors, and furniture. Each static path is characterized by an attenuation $\rho_{i,j}^S$ and delay τ_i^S . In addition, $H_{i,j,k}^X$ represents the CFR of dynamic paths induced by moving objects, each described by attenuation $\rho_{i,j,k}^X$, delay τ^X , Doppler frequency shift f^D , and AoA θ_k^X . We assume a uniform linear array where the antenna spacing is set to half of the wavelength. Δt denotes the CSI sample interval, which determines the temporal sampling resolution for Doppler estimation. The static and dynamic CFRs jointly encode the multipath delay, Doppler, and AoA across subcarriers, time, and antennas, forming the foundation for extracting delay-Doppler-AoA sensing features.

2.2 CSI Power Modelling

According to Eq. (1), the CSI can be multiplied by its complex conjugate to obtain the CSI power, which removes random phase components while implicitly retaining variations induced by underlying phase evolution,

$$\begin{aligned} P_{i,j,k} &= CSI_{i,j,k} \overline{CSI}_{i,j,k} \\ &= \alpha^2 (H_{i,j}^S + H_{i,j,k}^X) (\overline{H}_{i,j}^S + \overline{H}_{i,j,k}^X) \\ &= \alpha^2 \left[|H_{i,j}^S|^2 + |H_{i,j,k}^X|^2 + 2 \left| H_{i,j}^S \overline{H}_{i,j,k}^X \right| \cos \left(\angle H_{i,j}^S \overline{H}_{i,j,k}^X \right) \right], \end{aligned} \quad (3)$$

where $|\cdot|$ denotes the magnitude, and the TO, CFO, and PO are all eliminated. We then rely on Eq. (2) to obtain

$$\begin{aligned} &|H_{i,j}^S H_{i,j,k}^X| \cos (\angle H_{i,j}^S H_{i,j,k}^X) = \\ &\sum_{l_1} \sum_{l_2} \rho_{i,j}^S[l_1] \rho_{i,j,k}^X[l_2] \cos (\varphi_k^{\text{Doppler}}[l_2] + \varphi^{\text{Delay}}[l_1, l_2] + \varphi_{i,j}^{\text{AoA}}[l_1, l_2]), \end{aligned} \quad (4)$$

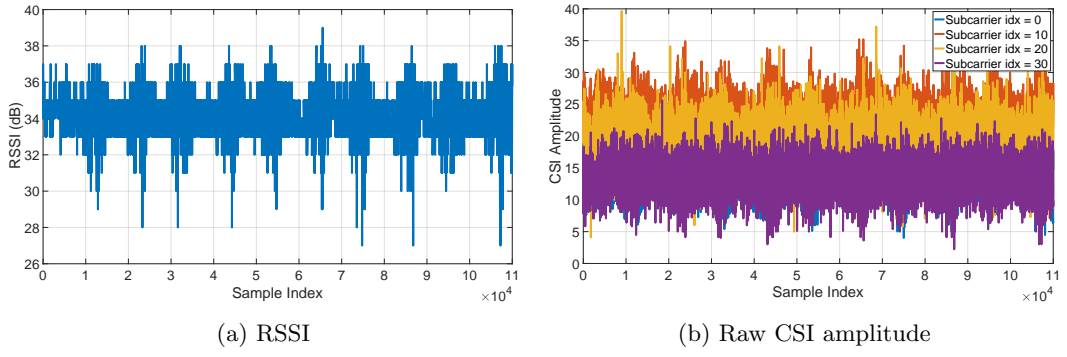


Fig. 1: Comparison of RSSI and CSI during human motion.

where

$$\begin{cases} \varphi_k^{\text{Doppler}}[l_2] = 2\pi f^D[l_2] (k-1) \Delta t, \\ \varphi_j^{\text{Delay}}[l_1, l_2] = 2\pi f_j (\tau^X[l_2] - \tau^S[l_1]), \\ \varphi_{i,j}^{\text{AoA}}[l_1, l_2] = \pi (i-1) (\sin \theta^X[l_2] - \sin \theta^S[l_1]). \end{cases} \quad (5)$$

From the above equations, it can be observed that the static component $H_{i,j}^S$ contains the direct propagation path between the transmitter and receiver, and its power $|H_{i,j}^S|^2$ typically dominates over other reflections. Furthermore, the mixed term $|H_{i,j}^S \bar{H}_{i,j,k}^X|$, which captures the interaction between the static and dynamic components, often remains stronger than the purely dynamic reflection term $|H_{i,j,k}^X|^2$. Therefore, the latter can be typically treated as noise in subsequent processing.

2.3 RSSI Derivation from CSI Power

We consider an approximate mapping from CSI power to RSSI. Let η denote an effective power-scaling factor that accounts for transmit power, receiver gains, and other RF-related losses. Under the common assumption that such factors vary slowly compared with channel fluctuations, η is treated as constant. Accordingly, the linear-scale RSSI (in milliwatts) $\mathcal{R}_{i,k}$ measured at the i -th antenna and the k -th time can be approximated from CSI power as

$$\mathcal{R}_{i,k} \approx \frac{1}{L} \sum_{j=1}^L \eta |P_{i,j,k}|, \quad (6)$$

where L is the number of subcarriers. It can be converted from the hardware-reported RSSI measurement (in dB) to a linear scale as $\mathcal{R} = 10^{\frac{\text{RSSI}_{\text{dB}}}{10}}$. Note that in our subsequent experiments, we use the Intel 5300 NIC, for which the reported RSSI_{dB} values are logarithmic power indicators expressed in dB [29], rather than absolute received power in dBm as commonly used in practical WiFi devices. This distinction affects only the absolute power reference and does not alter the linear conversion, since both dB and dBm follow the same logarithmic relationship up to a constant offset.

In commercial WiFi hardware, RSSI is quantized into integer steps with a resolution of about 0.5-1 dB. It is obtained by averaging the received signal power over a short interval within each packet, typically during the OFDM preamble, thereby yielding a packet-level and relatively stable power measurement, as opposed to the rapidly varying per-symbol amplitudes available in CSI. Due to this quantization, the effective amplitude resolution is limited to roughly 10-12 distinguishable levels per decade of received power. Moreover, RSSI reflects the total received power integrated across the entire communication bandwidth (e.g., 20 MHz), resulting in lower temporal and spectral resolution compared with subcarrier-resolved CSI. Fig. 1a and Fig. 1b show the reported RSSI (in dB) and the raw CSI amplitudes across selected subcarriers, including AGC-induced variations, measured by the Intel 5300 NIC, when a human subject repeatedly moves along an elliptical trajectory. RSSI mainly captures large-scale power variations correlated with CSI measurements, whereas CSI amplitudes provide higher-resolution signal details essential for fine-grained sensing. As indicated by the signal model in Section II-B, sensing information is preserved in the CSI power, and thus RSSI computed from the CSI power retains coarse sensing information, which is further validated below.

3 Passive Human Tracking via RSSI

This section presents the overall processing pipeline, outlining how RSSI can be transformed into Doppler-AoA features, delay estimates, and finally continuous trajectories.

3.1 System Overview

This work re-examines the physical-layer foundations of RSSI and shows that, when properly processed, RSSI can be effectively leveraged for sensing. Building upon these insights, we develop *WiRSSI*, a passive tracking framework that relies solely on low-resolution RSSI measurements for passive human tracking. The system adopts a bistatic 1Tx-3Rx configuration, while remaining naturally scalable to MIMO deployments. Despite the coarse resolution of RSSI, the proposed pipeline enables reliable AoA and delay estimation, and ultimately robust target tracking. The proposed WiRSSI framework consists of four main components:

- 1) *Static Clutter Removal*: Convert RSSI to linear scale, suppress the dominant static component, and extract motion-induced variations.
- 2) *Doppler-AoA Feature Extraction*: Apply sequential temporal and spatial FFTs to obtain a 2D Doppler-AoA spectrum and identify the target-induced peak.
- 3) *Delay Estimation*: Estimate the human-reflection delay by leveraging the amplitude ratio between the dynamic and static signal components.
- 4) *Localization and Tracking*: Convert the estimated delay and AoA into Cartesian coordinates and apply window-based filtering to obtain smoothed target trajectories.

3.2 Static Clutter Removal

Within a CPI, the RSSI measurements can be denoted as $\mathbf{R} \in \mathbb{R}^{N \times M}$, where N and M are the number of receiving antennas and RSSI samples, respectively. Each RSSI value is first converted to the linear power domain for subsequent processing. As discussed earlier, both the transmit power and the amplitude of each propagation path typically remain constant within the CPI. And it is reasonable to assume that the static component between the transmitter and receiver is dominant, as it corresponds to the LOS or strong NLOS propagation paths, whereas the dynamic component induced by moving targets typically propagates over longer and more attenuated paths. Under these assumptions, we compute the temporal mean of the RSSI at each antenna to suppress the static clutter, denoted by \mathcal{R}_i^S ,

$$\mathcal{R}_i^S \approx \frac{1}{M} \sum_{k=1}^M \mathcal{R}_{i,k}. \quad (7)$$

And the dynamic component is then extracted by subtracting the mean from the instantaneous RSSI:

$$\mathcal{R}_{i,k}^X \approx \mathcal{R}_{i,k} - \mathcal{R}_i^S. \quad (8)$$

This approach robustly suppresses static clutter concentrated at zero Doppler frequency with low computational complexity.

Furthermore, the dynamic component is normalized by the average \mathcal{R}_i^S :

$$\Delta \mathcal{R}_{i,k} = \frac{\mathcal{R}_{i,k}^X}{\mathcal{R}_i^S}. \quad (9)$$

This normalization mitigates unknown amplitude-related variations, including those caused by hardware imperfections and transmit power fluctuations, and facilitates subsequent delay estimation, which will be detailed in Section III.D.

3.3 Doppler-AoA Estimation via 2D FFT

The Doppler-AoA features are then obtained by applying 2D FFTs along the temporal and spatial dimensions, achieving low computational complexity and stable feature extraction.

3.3.1 Doppler FFT

First, a Doppler FFT is applied over the sampling time for each antenna:

$$\begin{aligned} X_i(f^D) &= \mathcal{F}_D\{\Delta \mathcal{R}_{i,k}\} \\ &= \sum_{k=0}^{M-1} \Delta \mathcal{R}_{i,k} e^{-j2\pi f^D (k-1)\Delta t}, \end{aligned} \quad (10)$$

where the Doppler frequency range is set within $\pm f_{\max}$, with $f_{\max} = v_{\max}/\lambda$ and v_{\max} denoting the maximum target Doppler velocity. A Doppler range of ± 100 Hz is used, corresponding to a maximum velocity of about 6 m/s at a 5 GHz center frequency, which adequately covers indoor human motion.

3.3.2 AoA FFT

An AoA FFT is applied over the antenna dimension at each Doppler bin to extract angle information:

$$\begin{aligned} Y(f^D, \theta^X) &= \mathcal{F}_{AoA}\{X_i(f^D)\} \\ &= \sum_{i=0}^{N-1} \left[X_i(f^D) e^{\mathbf{J}\pi(i-1) \sin \theta^S} \right] e^{-\mathbf{J}\pi(i-1) \sin \theta^X}, \end{aligned} \quad (11)$$

where θ^S denotes the AoA of the transmitter with respect to the receiver's linear antenna array, which can be pre-determined from the known antenna geometry. Meanwhile, since RSSI is real-valued, the Doppler FFT suffers from inherent spectral ambiguity. By incorporating θ^S , a constant spatial phase offset is introduced across antennas, which reshapes the joint Doppler-AoA spectrum and breaks this mirror symmetry (see Appendix A). To ensure unambiguous AoA estimation, the transmitter direction is configured to avoid being perpendicular to the receiver array axis (i.e., $\theta^S \neq 0^\circ$).

3.3.3 Doppler-AoA Spectrum

The resulting 2D spectrum $|Y(f^D, \theta^X)|$ characterizes the power distribution over Doppler and AoA. Let $\mathbf{Y} \in \mathbb{C}^{L_{\text{Doppler}} \times L_{\text{AoA}}}$ denote the Doppler-AoA matrix, where L_{Doppler} and L_{AoA} are the numbers of Doppler and angular bins, respectively. The location of each peak corresponds to a moving target, capturing its radial motion through Doppler and its spatial direction through AoA.

3.4 Delay Estimation from Signal Amplitude

Unlike CSI, which enables delay estimation via subcarrier phase information, RSSI aggregates power over the entire bandwidth and thus lacks the phase information required for conventional delay extraction. To address this limitation, we instead explore the use of signal amplitude as an alternative cue for delay estimation. However, beyond its dependence on propagation distance, the amplitude of each propagation path is jointly influenced by multiple factors, including the target reflection coefficient, incident angle, surface material, and antenna polarization. These factors complicate the direct use of raw amplitude measurements for accurate sensing.

3.4.1 Amplitude Modeling of Static and Dynamic Paths

We first briefly explain the rationale for exploiting the path amplitude to infer the propagation delay. From a propagation perspective, the received signal amplitude inherently depends on the propagation distance due to path-loss and attenuation effects. Since the propagation delay is directly proportional to the path length, the amplitude provides an indirect yet informative cue for delay estimation. According to the amplitude-delay dependence derived in Appendix B and Appendix C, the amplitudes of the dominant static Tx-Rx path and the target-induced dynamic path can be expressed as

$$\begin{cases} \rho^S = \frac{\Gamma^S}{\tau^{T \rightarrow R}}, \\ \rho^X = \frac{\tilde{\Gamma}^X}{\tau^{T \rightarrow X} + \tau^{X \rightarrow R}}, \end{cases} \quad (12)$$

where $\tau^{T \rightarrow R}$ denotes the propagation delay of the static Tx-Rx path, and $\tau^{T \rightarrow X}$ and $\tau^{X \rightarrow R}$ are the propagation delays from the transmitter to the target and from the target to the receiver, respectively. The coefficients Γ^S and $\tilde{\Gamma}^X$ capture path-dependent amplitude factors, including reflection characteristics, antenna gains, polarization effects, and other hardware-related terms.

In particular, Appendix C also shows that the dynamic-path amplitude can be decomposed into a slowly varying geometric term and a reflection-related term. Specifically, we write

$$\tilde{\Gamma}^X \triangleq \frac{\tau^{T \rightarrow X} + \tau^{X \rightarrow R}}{\tau^{T \rightarrow X} \tau^{X \rightarrow R}} \Gamma^X, \quad (13)$$

where Γ^X denotes a delay-independent amplitude factor associated with the target's scattering characteristics. Since these characteristics, together with the underlying hardware effects, vary on a much slower time scale

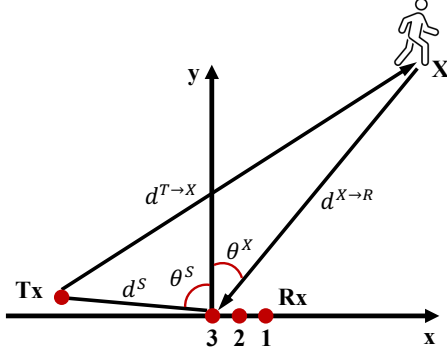


Fig. 2: Bistatic geometry of the 1Tx-3Rx WiFi setup.

than the propagation delays induced by target motion, Γ^X can be treated as quasi-static. Moreover, for a fixed transceiver setup and a target whose motion is confined to a finite region relative to the Tx-Rx separation, the delay ratio $(\tau_k^{T \rightarrow X} + \tau_k^{X \rightarrow R})/(\tau_k^{T \rightarrow X} \tau_k^{X \rightarrow R})$ varies much more slowly over time than the total bistatic delay $\tau_k^{T \rightarrow X} + \tau_k^{X \rightarrow R}$. As a result, the combined coefficient $\tilde{\Gamma}_k^X$ can be approximated as a constant in typical indoor tracking scenarios.

3.4.2 Delay Estimation

Recall from Eq. (11) that, under the single-target assumption, the dominant peak in the extracted 2D Doppler-AoA spectrum corresponds to the moving target. Accordingly, the amplitude at the Doppler-AoA bin (f^D, θ^X) reflects the contribution of the target-induced dynamic path. In contrast, the static component is assumed to be dominated by the LoS Tx-Rx path. Using the amplitude models in (12), the ratio between the static and dynamic path amplitudes can be expressed as

$$|Y(f^D, \theta^X)| = \frac{\rho^X}{\rho^S} = \frac{\tilde{\Gamma}^X}{\Gamma^S} \frac{\tau^{T \rightarrow R}}{\tau^X}, \quad (14)$$

where $\tau^X \triangleq \tau^{T \rightarrow X} + \tau^{X \rightarrow R}$ denotes the total bistatic propagation delay. Under the above approximation, the reflection-coefficient ratio $\gamma \triangleq \tilde{\Gamma}^X/\Gamma^S$ can be treated as a constant and obtained through prior calibration, as detailed below. This ratio effectively absorbs and cancels hardware-dependent amplitude scaling effects, thereby improving robustness across different devices and deployment configurations. In addition, the static-path delay $\tau^{T \rightarrow R}$ can be measured in advance. Consequently, the bistatic delay τ^X associated with the target-induced reflection path can be directly inferred.

3.4.3 Prior Calibration of Reflection Coefficient Ratio

The reflection-coefficient ratio γ is obtained through a one-time calibration under the same Tx-Rx deployment. During calibration, the bistatic delay of the target-induced path, $\tau^X = \tau^{T \rightarrow X} + \tau^{X \rightarrow R}$, is measured using an auxiliary ranging modality that provides accurate position information, such as a co-located mmWave radar. The static-path delay $\tau^{T \rightarrow R}$ is measured in advance. By collecting measurements at multiple known target locations within the sensing area, γ is estimated at each location, and the final calibration value is obtained by averaging these estimates. During subsequent localization and tracking, the pre-estimated ratio γ is treated as a known parameter and used to infer the bistatic delay associated with the human-reflection path.

3.5 Object Localization and Tracking

3.5.1 Object Localization

As shown in Fig. 2, the estimated polar coordinates of each detection, including the delay and the AoA, are first converted into Cartesian coordinates for target localization. Let $d^{T \rightarrow X}$ and $d^{X \rightarrow R}$ denote the propagation distances from the transmitter to the target and from the target to the receiver, respectively. These distances are obtained from the corresponding delays $\tau^{T \rightarrow X}$ and $\tau^{X \rightarrow R}$ by multiplying with the speed of light.

Given the estimated AoA θ^X of the target-induced reflection and the known Tx-Rx separation, the target-receiver distance $d^{X \rightarrow R}$ can be computed according to the law of cosines as

$$d^{X \rightarrow R} = \frac{(d^X)^2 - (d^S)^2}{2[d^X - d^S \cos(\theta^X - \theta^S)]}. \quad (15)$$

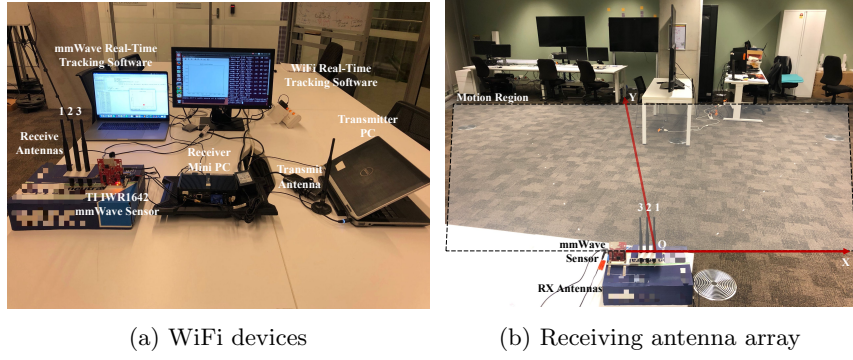


Fig. 3: Experimental setup of the WiFi sensing system.

Then, the target coordinate can be represented in the receiver's local Cartesian coordinate system as:

$$\begin{cases} x = d^{X \rightarrow R} \sin \theta^X, \\ y = d^{X \rightarrow R} \cos \theta^X. \end{cases} \quad (16)$$

3.5.2 Object Tracking

Before performing continuous tracking, the per-frame position estimates may contain outliers. To mitigate these effects, a Hampel filter is first applied to identify and remove outliers in both the X- and Y- coordinates. After that, a Savitzky-Golay (SG) filter is used to smooth the remaining position sequence, producing a locally smoothed trajectory while preserving the underlying motion trend. Unlike some CSI-based systems [4, 24] that employ an Extended Kalman Filter (EKF) to jointly refine delay, AoA, and Doppler, applying EKF in RSSI-based sensing is challenging due to the high noise level in Doppler estimates, as will be discussed in Section V. Such noisy Doppler measurements can destabilize the EKF update process. The proposed window-based smoothing approach avoids this issue and provides robust, temporally consistent tracking results.

4 Implementation

4.0.1 WiFi Dataset

As shown in Fig. 3, the WiFi dataset is collected using two PCs equipped with Intel 5300 NICs, configured in a 1Tx-3Rx setting and serving as the transmitter and receiver, respectively. The system operates at a center frequency of 5.32 GHz, with the transmitter and receiver separated by approximately 2.3 m. The Linux 802.11n CSI Tool [29] is configured in monitor mode with a sampling rate of 1 kHz. *Both CSI and RSSI can be simultaneously recorded.* The dataset contains three representative motion trajectories: (1) Elliptical Track, (2) Linear Track, and (3) Rectangular Track, as illustrated in Fig. 4a, Fig. 4b, and Fig. 4c, respectively. A human subject moves at an average walking speed of approximately 1 m/s within the monitored area during data collection.

4.0.2 Default Configuration

Each CPI contains 128 RSSI samples per Rx antenna. A step size of 32 samples (approximately 32 ms between consecutive CPIs) is used, resulting in an overlap of 96 samples between adjacent CPIs. The AoA domain is discretized into 64 bins spanning $[-90^\circ, 90^\circ]$, corresponding to an angular resolution of approximately 2.8° near broadside. For Doppler estimation, 128 Doppler bins are used over the range of $[-100, 100]$ Hz, yielding a Doppler resolution of approximately 1.56 Hz. The low computational complexity of the FFT-based processing ensures that the average processing time per CPI remains shorter than the step-size interval, enabling real-time operation. For trajectory refinement, outlier suppression is performed using a 1D Hampel filter with a window size of 7 and a threshold of 1 standard deviation. The denoised sequence is then smoothed using a SG filter with a window length of 101 (about 3s of estimated data) and a polynomial order of 2.

4.0.3 Baseline

For performance comparison, we consider two representative CSI-based sensing methods: SRCC [10] and CASR [11, 21]. The SRCC method estimates delay, AoA, and Doppler parameters by constructing a per-antenna reference signal to eliminate random phase distortions, followed by delay-domain beamforming and Doppler-AoA 2D FFT for parameter extraction. Importantly, this process does not require any prior hardware calibration, enabling accurate and robust parameter estimation. The estimated trajectories are used to compared with the

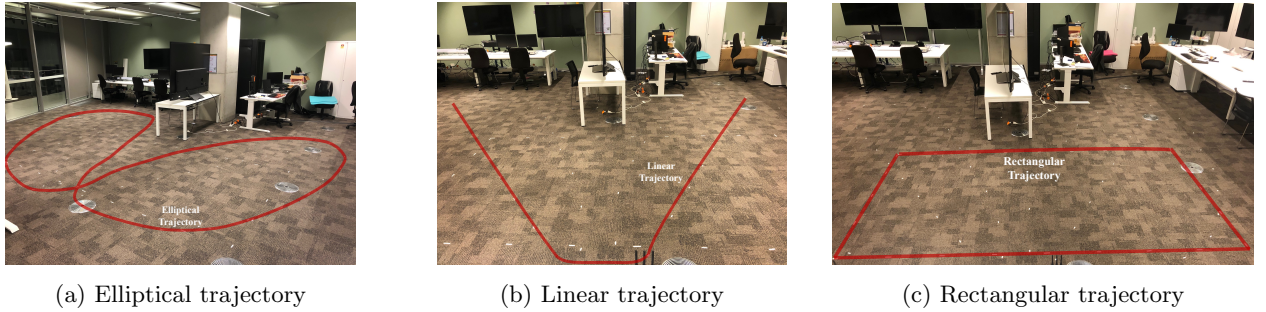


Fig. 4: Human motion trajectories: (a) elliptical, (b) linear, and (c) rectangular.

RSSI-based results. In addition, CASR removes random phase offsets by forming ratios between CSI measurements from two antennas. Based on the CSI-ratio signal, we apply a Doppler-Delay 2D FFT to estimate Doppler and propagation delay (range). However, due to residual hardware-induced phase inconsistencies across antennas, accurate AoA estimation is challenging for CASR. Therefore, we report only Doppler and range results for comparison. The ground-truth trajectories with centimeter-level accuracy are obtained using a TI IWR1642 mmWave radar [30].

5 Results

This section presents the experimental results of WiRSSI, including comparisons with a CSI-based baseline, overall tracking accuracy, reflection-coefficient estimation, and the impact of transceiver separation and CPI size.

5.1 Comparison with CSI-based Method

We first compare the performance of the proposed WiRSSI against the CSI-based baselines in terms of Doppler, AoA, and delay estimation. All CSI-derived features are processed using the same configuration for fair comparison.

5.1.1 AoA Estimation

Fig. 5a, Fig. 6a, and Fig. 7a compare RSSI-based AoA estimates with the ground-truth mmWave radar measurements, while Fig. 5b, Fig. 6b, and Fig. 7b compare CSI-based AoA estimates with the same ground truth. Due to the coarse resolution of RSSI, the RSSI-derived AoA traces exhibit larger fluctuations and more outliers compared with the CSI-based results. Nevertheless, the dominant angular trend extracted from RSSI still closely follows the ground-truth trajectory across all motion patterns, indicating that the proposed Doppler-AoA processing can recover reliable directional information even under low-resolution measurements. It is also observed that RSSI relies solely on the Tx-Rx geometric AoA (θ^S) to suppress Doppler-AoA mirror ambiguities, whereas CSI leverages both spatial- and spectral-domain phase information to jointly constrain the angle estimation and remove mirrored components. Overall, while CSI provides cleaner and more stable AoA estimates, RSSI still retains sufficient angular consistency to support accurate trajectory tracking.

5.1.2 Delay Estimation

Fig. 5c, Fig. 6c, and Fig. 7c compare RSSI-based range variation estimates with the mmWave radar ground truth, while Fig. 5d, Fig. 6d, and Fig. 7d compare the corresponding CSI-based results. Here, the range represents the distance difference between the Tx-target-Rx reflection path and the direct Tx-Rx path. Because RSSI integrates power over the entire channel bandwidth, it loses the subcarrier-dependent phase diversity typically required for delay estimation in CSI-based sensing. Surprisingly, the amplitude-based delay estimation derived from RSSI achieves results that are highly consistent with the ground truth, which is often overlooked in prior work. This capability arises from the power-delay relationship exploited in Section III, although it requires pre-measuring the reflection coefficient ratio. In contrast, CSI naturally preserves subcarrier-level phase information and can recover propagation delay directly without prior calibration. In the CSI-based implementation, the range is searched from 0 to 32 m and uniformly discretized into 128 bins, yielding a range resolution of 0.25 m. However, in the CASR method, the nonlinear transformation applied across subcarriers introduces noticeable delay distortion, as indicated by the red points. By contrast, the SRCC method (shown in blue) relies on linear processing and preserves the intrinsic subcarrier structure, thereby achieving more accurate delay estimation. The results show that despite lacking phase information, the RSSI-based amplitude method is still able to capture the overall range evolution.

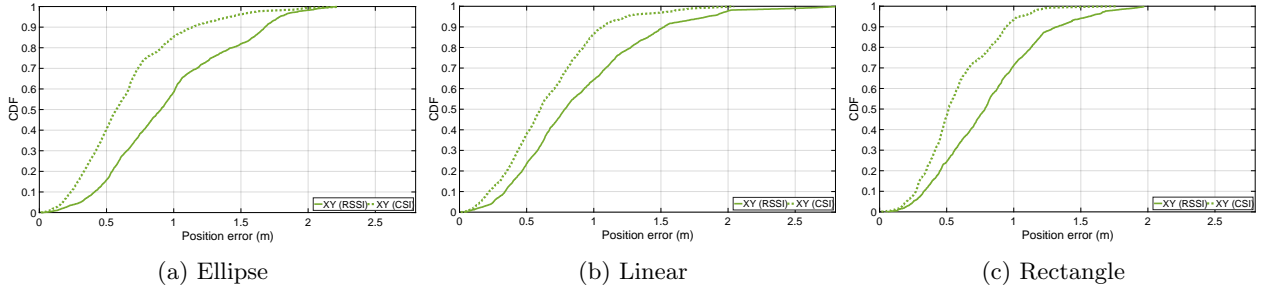


Fig. 8: CDFs of trajectory errors.

Table 1: Median (CDF=0.5) and 80% (CDF=0.8) position errors of smoothed RSSI and CSI results under different trajectories.

Trajectory	RSSI Error (m)			CSI Error (m)		
	X	Y	XY	X	Y	XY
CDF = 0.5						
Ellipse	0.492	0.607	0.905	0.386	0.318	0.574
Linear	0.312	0.667	0.784	0.378	0.342	0.599
Rectangle	0.321	0.627	0.785	0.407	0.218	0.514
CDF = 0.8						
Ellipse	0.923	1.076	1.432	0.714	0.590	0.909
Linear	0.684	1.053	1.275	0.692	0.659	0.923
Rectangle	0.579	0.910	1.129	0.588	0.452	0.826

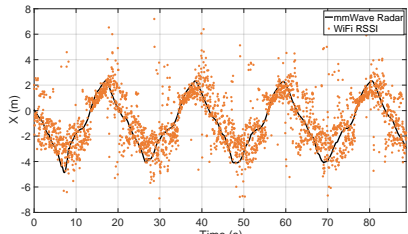
5.1.3 Doppler Estimation

Fig. 5e, Fig. 6e, and Fig. 7e compare RSSI-based Doppler trace estimates with the bistatic Doppler derived from the mmWave radar ground truth, while Fig. 5f, Fig. 6f, and Fig. 7f compare the corresponding CSI-based results. It is worth noting that human motion produces multiple Doppler components due to different body parts (e.g., legs, arms, and torso), and the dominant component may vary over time. The mmWave-derived bistatic Doppler therefore represents an overall motion trend, and slight discrepancies between WiFi and mmWave observations are expected. The Doppler extracted from RSSI exhibits irregular temporal patterns and is strongly affected by coarse amplitude quantization and limited resolution. Consequently, the RSSI-based Doppler estimates are noisy and fail to clearly reveal the underlying periodic motion. In contrast, CSI-based Doppler estimation yields significantly cleaner and more stable traces that closely follow the mmWave-derived Doppler across different motion trajectories. Both SRCC and CASR produce comparable Doppler estimation performance, highlighting the advantage of preserving fine-grained CSI information for Doppler sensing.

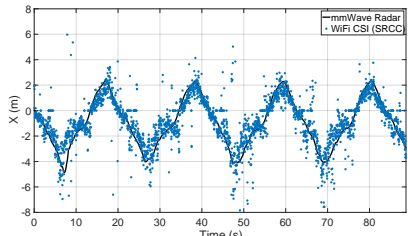
5.2 Overall Tracking Accuracy

Fig. 8 and Table 1 summarize the overall tracking accuracy of WiRSSI under three trajectories. The CDF curves indicate that RSSI-based tracking achieves sub-meter median accuracy across all motion patterns. The median XY errors (CDF = 0.5) are 0.905 m, 0.784 m, and 0.785 m, respectively. These results show that, despite the coarse resolution of RSSI, the proposed processing pipeline can reliably recover human motion at meter-level precision. As expected, CSI-based tracking provides higher accuracy due to its finer resolution. The corresponding median XY errors are 0.574 m, 0.599 m, and 0.514 m. Overall, CSI achieves higher tracking accuracy than RSSI, reducing the median XY error by about 0.26 m on average across the three trajectories.

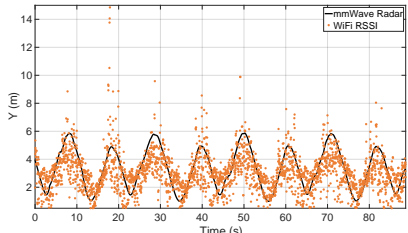
To provide a clearer illustration of the estimated trajectories, Fig. 9, Fig. 10, and Fig. 11 present the X- and Y-coordinate estimates before and after smoothing. As shown, the raw RSSI-based coordinates exhibit substantial noise and wide scattering, whereas the raw CSI-based coordinates are more concentrated. After applying the Hampel outlier removal and SG smoothing, both RSSI and CSI trajectories align closely with the mmWave radar ground truth. The RSSI traces, in particular, show a dramatic reduction in jitter and reveal a clear motion trend. These observations confirm the effectiveness of the proposed RSSI preprocessing and smoothing strategy in improving trajectory stability and consistency. In addition, Fig. 12, Fig. 13, and Fig. 14 visualize the reconstructed 2D trajectories, respectively. The RSSI-based trajectories exhibit larger deviations and local distortions, but the overall motion shape is still preserved. In contrast, CSI-based trajectories follow the mmWave ground truth more closely. Overall, these results demonstrate that WiRSSI enables meaningful trajectory tracking using only RSSI measurements.



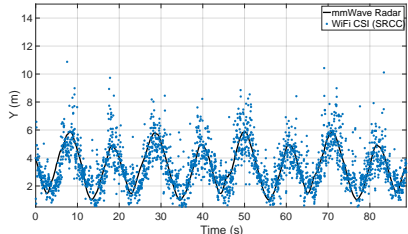
(a) Raw x-axis coordinate (RSSI)



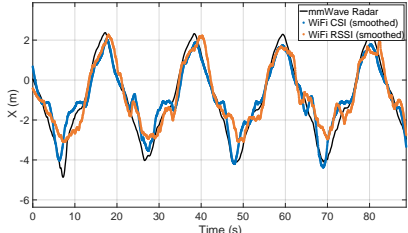
(b) Raw x-axis coordinate (CSI)



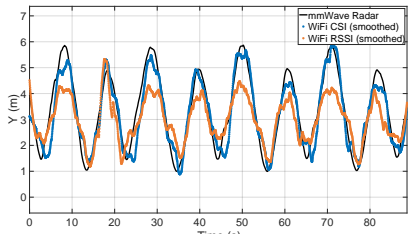
(c) Raw y-axis coordinate (RSSI)



(d) Raw y-axis coordinate (CSI)

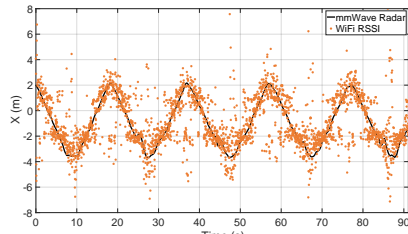


(e) Smoothed x-axis coordinate

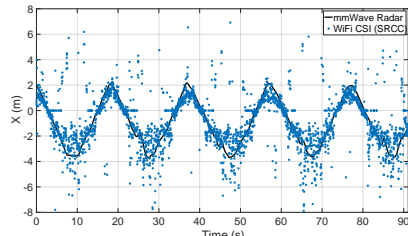


(f) Smoothed y-axis coordinate

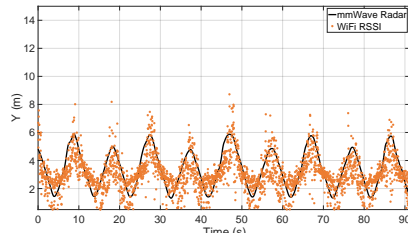
Fig. 9: Elliptical trajectory.



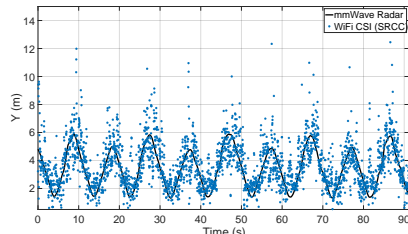
(a) Raw x-axis coordinate (RSSI)



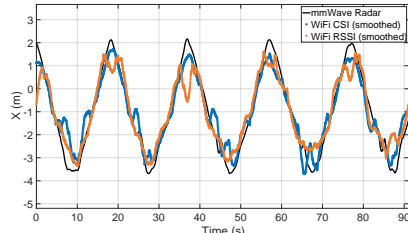
(b) Raw x-axis coordinate (CSI)



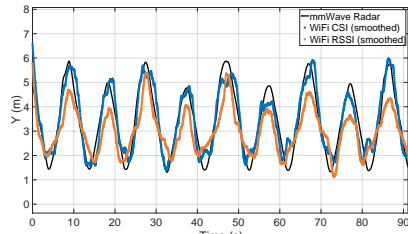
(c) Raw y-axis coordinate (RSSI)



(d) Raw y-axis coordinate (CSI)

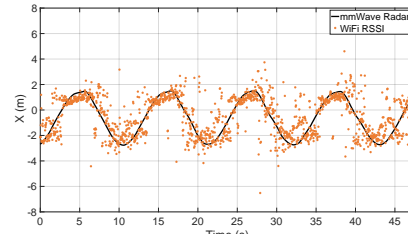


(e) Smoothed x-axis coordinate

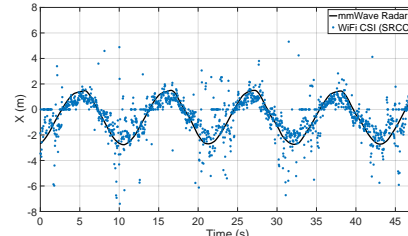


(f) Smoothed y-axis coordinate

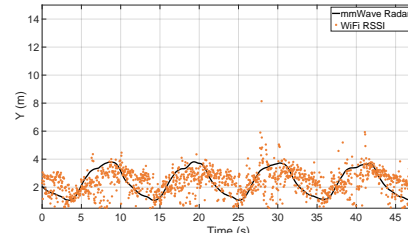
Fig. 10: Linear trajectory.



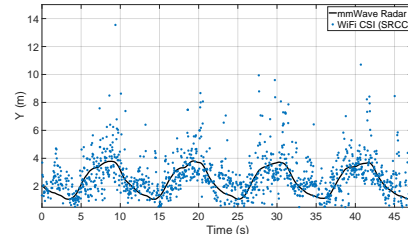
(a) Raw x-axis coordinate (RSSI)



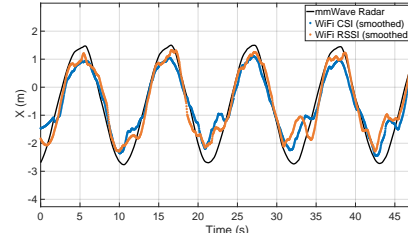
(b) Raw x-axis coordinate (CSI)



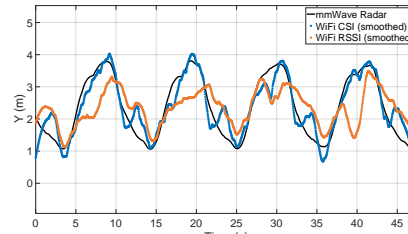
(c) Raw y-axis coordinate (RSSI)



(d) Raw y-axis coordinate (CSI)

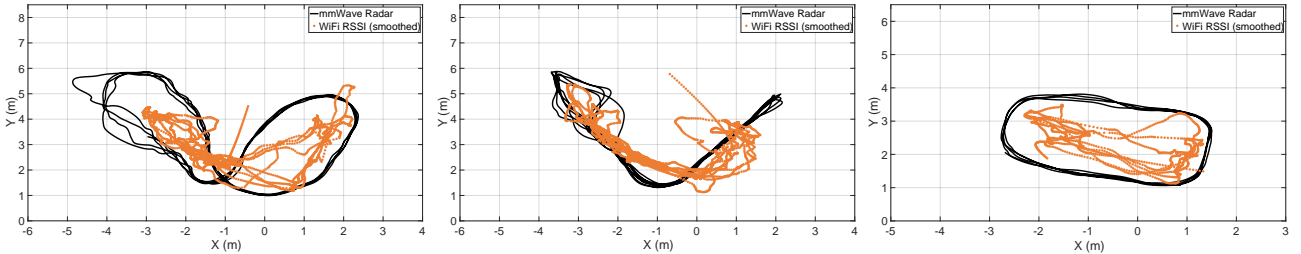


(e) Smoothed x-axis coordinate



(f) Smoothed y-axis coordinate

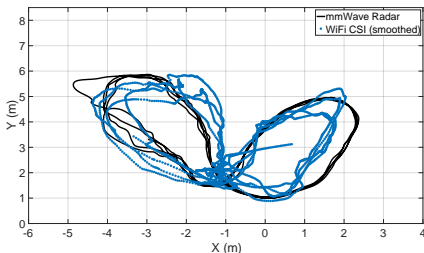
Fig. 11: Rectangular trajectory.



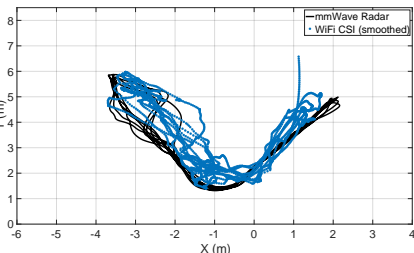
(a) RSSI

(a) RSSI

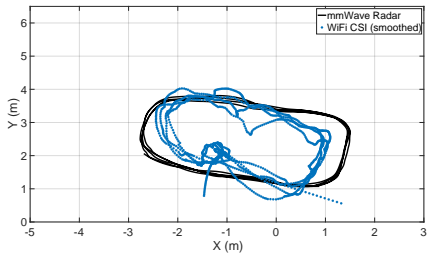
(a) RSSI



(b) CSI



(b) CSI



(b) CSI

Fig. 12: Elliptical trajectory.

Fig. 13: Linear trajectory.

Fig. 14: Rectangular trajectory.

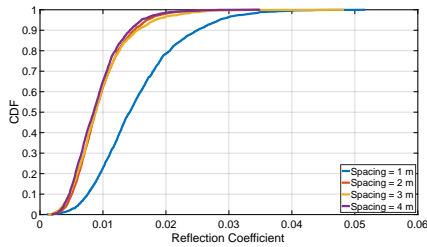


Fig. 15: Reflection coefficient.

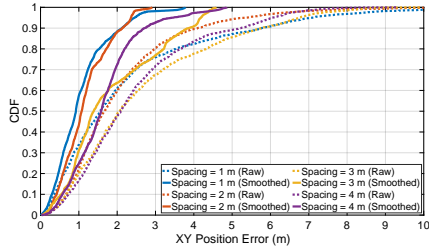


Fig. 16: Impact of Tx-Rx distance.

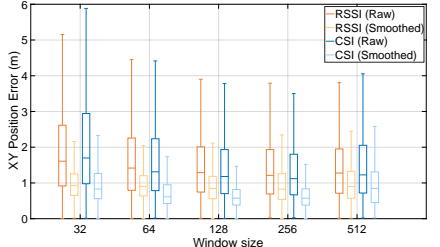


Fig. 17: Impact of CPI size.

5.3 Human Reflection Coefficient Estimation

Fig. 15 presents the estimated reflection coefficient ratio γ for different Tx-Rx spacings (1-4 m) and across multiple subjects. For Tx-Rx spacings of 2-4 m, the distribution of γ is highly concentrated, with median values around 0.01 and a variance of approximately 0.004. This indicates that, in typical mid-range Tx-Rx deployments, the human reflection coefficient remains relatively stable across different subjects and motions. In contrast, when the Tx-Rx spacing is reduced to 1 m, the estimated γ increases noticeably, with a median value around 0.015 and a visibly larger spread. This result is consistent with the analysis in Appendix C. Specifically, when the transmitter and receiver are close, the bistatic delay ratio $(\tau^{T \rightarrow X} + \tau^{X \rightarrow R}) / (\tau^{T \rightarrow X} \cdot \tau^{X \rightarrow R})$ becomes more sensitive to target position changes. As a result, the geometry-dependent term absorbed into γ exhibits larger variations, leading to increased uncertainty in the estimated reflection coefficient. Overall, these results indicate that a pre-calibrated reflection coefficient ratio is feasible for amplitude-based delay estimation when the Tx-Rx spacing is not excessively small. Moderate Tx-Rx separations (e.g., 2-4 m) provide a favorable trade-off between maintaining a dominant propagation path and ensuring the stability of γ .

5.4 Impact of Tx-Rx Distance

Fig. 16 illustrates the raw and smoothed XY tracking errors for Tx-Rx spacings ranging from 1 to 4 m. As the spacing increases, the tracking error gradually rises, primarily due to the increased impact of environmental multipath propagation. With larger separations, reflections from walls, floors, and surrounding objects become more prominent relative to the direct path, weakening the dominance of the static Tx-Rx component. In addition, the increased propagation distance leads to higher attenuation and noise, further degrading the reliability of AoA and delay estimation. Nevertheless, the proposed RSSI-based sensing approach remains robust under increased multipath interference.

5.5 Impact of CPI Size

Fig. 17 shows the XY tracking errors for CPI sizes ranging from 32 to 512 samples. Overall, both RSSI- and CSI-based tracking benefit from increasing the CPI size, as larger windows improve Doppler resolution and

suppress short-term fluctuations. For RSSI, the smoothed median error decreases from 0.925 m at 32 samples to 0.824 m at 256 samples, after which the improvement saturates and slightly degrades at 512 samples (0.899 m). This suggests that while longer windows enhance Doppler-AoA stability, excessively large CPIs blur fast motion dynamics. A similar trend is observed for CSI. Consequently, a moderate CPI size (128-256 samples) provides a favorable trade-off for accurate sensing.

6 Discussion

This work challenges the prevailing perception that RSSI is inherently unsuitable for fine-grained WiFi sensing. Rather than treating RSSI as a coarse indicator for signal strength or distance, our results demonstrate that RSSI, when interpreted through an appropriate power-domain model, can implicitly preserve motion-related information that is traditionally accessed through CSI. By consolidating the experimental observations, several key insights and trade-offs emerge.

6.1 Physical Basis of RSSI-based Sensing

A central finding of this work is that the sensing capability of RSSI originates from the interaction between the dominant static path and the target-induced dynamic path in the power domain in practical multipath environments. Although RSSI discards explicit phase information by aggregating power across subcarriers, the resulting cross-term encodes Doppler-, AoA-, and delay-dependent variations. As a result, meaningful motion signatures remain observable even under coarse quantization. In contrast to conventional RSSI models that rely solely on large-scale path loss, the proposed framework exploits these fine-grained amplitude fluctuations to infer geometric information associated with target motion.

6.2 Performance Gap Between RSSI and CSI

Experimental results consistently show that CSI-based sensing outperforms RSSI-based sensing in terms of accuracy, with an average median tracking error gap of approximately 0.26 m. This gap primarily stems from the loss of subcarrier-level phase diversity and the limited amplitude resolution of RSSI. In particular, Doppler estimation from RSSI is inherently noisier, which constrains target separability in the Doppler domain. Nevertheless, the RSSI-derived AoA and delay estimates exhibit sufficient temporal consistency to enable reliable trajectory reconstruction after lightweight smoothing. These observations suggest that RSSI does not aim to replace CSI, but rather complements it by offering a hardware-friendly alternative when CSI is unavailable or unreliable.

6.3 Practical Deployment Considerations

From a system perspective, the proposed WiRSSI is well suited for real-world deployment, as RSSI is ubiquitously available on commodity WiFi devices and the proposed FFT-based processing pipeline is computationally lightweight, enabling real-time operation without firmware or driver-level access. These properties make WiRSSI attractive for large-scale and low-cost deployments where CSI is unavailable. At the same time, performance degradation under strong multipath conditions and large Tx-Rx separations highlights the importance of environment-aware deployment and moderate spacing. The amplitude-based delay estimation relies on a reflection-coefficient ratio obtained through a brief pre-calibration step that must be repeated when the deployment configuration changes, due to its dependence on Tx-Rx geometry and the surrounding environment. In multi-target scenarios, the limited resolution and increased Doppler noise of RSSI constrain target separation primarily to the AoA domain; with a three-antenna array, at most two targets can be reliably resolved before extracting their corresponding delays for tracking. In contrast, CSI-based sensing enables joint discrimination across delay, Doppler, and AoA domains, offering greater scalability in complex scenes, while extending RSSI-based sensing to more challenging multi-target scenarios remains an important direction for future work.

6.4 Broader Implications for ISAC

Beyond RSSI-based sensing, the insights derived from this work have broader implications for ISAC. The results suggest that power-domain measurements can retain richer sensing information than commonly assumed when interpreted through appropriate signal models. This perspective may motivate new sensing paradigms that exploit aggregated or low-resolution measurements, thereby reducing hardware complexity and calibration requirements while maintaining acceptable sensing performance. Furthermore, the demonstrated relationship between RSSI and CSI power points to opportunities for hybrid sensing schemes that jointly leverage both measurements to enhance robustness and adaptability.

This discussion highlights that RSSI should not be viewed as a degraded substitute for CSI, but rather as a distinct sensing modality with its own strengths, limitations, and application niches.

7 Conclusion

This work revisits the long-held assumption that RSSI is too coarse for fine-grained WiFi sensing. By deriving a power-domain relationship between CSI power and RSSI, we develop *WiRSSI*, a bistatic passive tracking framework that extracts Doppler and AoA via lightweight 2D FFT processing and infers bistatic delay from an amplitude-delay relationship. The delay inference requires only a one-time calibration of a reflection-coefficient ratio. Extensive experiments show that WiRSSI achieves sub-meter median trajectory accuracy across multiple motion patterns, despite the low sensing resolution of RSSI. Overall, this study demonstrates that RSSI can enable effective passive tracking as a low-cost and hardware-friendly alternative for WiFi sensing.

Declarations

Funding

This research did not receive any specific grant from funding agencies in the public, commercial, or not-for-profit sectors.

Conflict of Interest

The authors declare no competing interests.

Data Availability

The datasets generated and analysed during the current study are available from the corresponding author on reasonable request and will be made publicly available upon acceptance of the manuscript.

Code Availability

The code used in this study is available from the corresponding author upon reasonable request.

Author Contributions

Z.W. conceived the study, developed the signal model and algorithms, conducted the experiments, and drafted the manuscript. J.A.Z. supervised the research, contributed to the technical analysis, and revised the manuscript. K.W. assisted with data analysis and contributed to manuscript revision. Y.J.G. provided overall guidance and contributed to the interpretation of the results. All authors reviewed and approved the final manuscript.

Appendix A Exploiting Transmitter AoA to Resolve Doppler-AoA Symmetry

For the RSSI measurements $\mathcal{R}_{i,k} \in \mathbb{R}$ at the i -th receiving antenna, the Doppler FFT

$$X_i(f^D) = \mathcal{F}_D\{\mathcal{R}_{i,k}\} \quad (\text{A1})$$

satisfies the conjugate-symmetry property:

$$X_i(-f^D) = \overline{X_i(f^D)}, \quad (\text{A2})$$

which implies same magnitudes at Doppler frequencies $\pm f^D$.

An AoA FFT is then applied across the antenna dimension:

$$Y(f^D, \theta^X) = \sum_{i=0}^{N-1} X_i(f^D) e^{-J\pi(i-1)(\sin \theta^X - \sin \theta^S)}. \quad (\text{A3})$$

where θ^S denotes the AoA of the transmitter relative to the receiver array.

Using the Doppler symmetry in (A2) and $\sin(-\theta^X) = -\sin\theta^X$, the response at $(-f^D, -\theta^X)$ becomes:

$$\begin{aligned} Y(-f^D, -\theta^X) &= \sum_{i=0}^{N-1} X_i(-f^D) e^{-J\pi(i-1)[\sin(-\theta^X) - \sin\theta^S]} \\ &= \sum_{i=0}^{N-1} \overline{X_i(f^D)} e^{-J\pi(i-1)(-\sin\theta^X - \sin\theta^S)}. \end{aligned} \quad (\text{A4})$$

To examine whether (f^D, θ^X) and $(-f^D, -\theta^X)$ form a conjugate-symmetric pair, we test whether there exists a global phase offset ϕ such that

$$Y(-f^D, -\theta^X) = e^{-J\phi} \overline{Y(f^D, \theta^X)} \quad (\text{A5})$$

Taking the conjugate of (A3) yields

$$\overline{Y(f^D, \theta^X)} = \sum_{i=0}^{N-1} \overline{X_i(f^D)} e^{J\pi(i-1)(\sin\theta^X - \sin\theta^S)}. \quad (\text{A6})$$

For (A4) and (A6) to match up to a global phase offset, the steering phases must satisfy:

$$\sin\theta^X + \sin\theta^S = \sin\theta^X - \sin\theta^S, \quad (\text{A7})$$

which reduces to $\sin\theta^S = 0$, i.e., $\theta^S = 0^\circ$ or 180° , corresponding to the special case where the transmitter-receiver direction is perpendicular to the array axis. Otherwise ($\theta^S \neq 0^\circ, 180^\circ$), the steering terms are not conjugate-symmetric, and the Doppler-AoA mirror symmetry is broken.

Appendix B Amplitude-Delay Relationship of the LOS Path

We first consider a LOS propagation path between a transmitter and a receiver. Let the corresponding propagation delay be denoted by $\tau^{T \rightarrow R}$. Under free-space propagation, the complex channel coefficient of the LOS path can be expressed as

$$h^{\text{LOS}} = \Gamma^S e^{-j2\pi f_c \tau^{T \rightarrow R}}, \quad (\text{B8})$$

where f_c denotes the carrier frequency. The coefficient Γ^S is a real-valued amplitude factor that absorbs transmit power, antenna gains, polarization mismatch, and other system- and hardware-dependent constants.

Taking the magnitude yields the LOS path amplitude

$$\rho^S \triangleq |h^{\text{LOS}}| = \frac{\Gamma^S}{\tau^{T \rightarrow R}}, \quad (\text{B9})$$

which reveals an inverse dependence between the received signal amplitude and the propagation delay.

Appendix C Amplitude-Delay Relationship of the NLOS Path

We next consider a NLOS propagation path induced by a human target. Although the target may generate distributed scattering, the received signal is typically dominated by a single effective reflection associated with the strongest scattering center. Accordingly, the NLOS propagation is modelled as a bistatic path consisting of two segments: from the transmitter to the target, and from the target to the receiver. Let $\tau^{T \rightarrow X}$ and $\tau^{X \rightarrow R}$ denote the propagation delays of the two segments, respectively. Following a multiplicative Green's-function-based formulation [16], the complex NLOS channel coefficient can be expressed as

$$h^{\text{NLOS}} = \Gamma^X \frac{e^{-J2\pi f_c (\tau^{T \rightarrow X} + \tau^{X \rightarrow R})}}{\tau^{T \rightarrow X} \tau^{X \rightarrow R}}, \quad (\text{C10})$$

where Γ^X is an effective reflection-related amplitude coefficient that captures target-dependent scattering characteristics, antenna gains, polarization effects, and other system- and hardware-related factors.

Taking the magnitude yields the NLOS path amplitude

$$\rho^X \triangleq |h^{\text{NLOS}}| = \frac{\Gamma^X}{\tau^{T \rightarrow X} \tau^{X \rightarrow R}}. \quad (\text{C11})$$

To relate the amplitude to the total bistatic delay, the inverse delay product can be rewritten as

$$\frac{1}{\tau^{T \rightarrow X} \tau^{X \rightarrow R}} = \frac{1}{\tau^{T \rightarrow X} + \tau^{X \rightarrow R}} \cdot \zeta, \quad (\text{C12})$$

where

$$\zeta \triangleq \frac{\tau^{T \rightarrow X} + \tau^{X \rightarrow R}}{\tau^{T \rightarrow X} \tau^{X \rightarrow R}} = \frac{1}{\tau^{T \rightarrow X}} + \frac{1}{\tau^{X \rightarrow R}} \quad (\text{C13})$$

is a geometry-dependent factor determined by the bistatic propagation geometry.

We next examine how the geometry-dependent factor ζ varies under target motion. When the target undergoes small displacements, the two propagation segments experience small delay variations $\Delta\tau_1$ and $\Delta\tau_2$. In this case, ζ defined in (C13) can be approximated by a first-order Taylor expansion as

$$\begin{aligned} \Delta\zeta &\approx \frac{\partial\zeta}{\partial\tau^{T \rightarrow X}} \Delta\tau_1 + \frac{\partial\zeta}{\partial\tau^{X \rightarrow R}} \Delta\tau_2 \\ &= -\frac{\Delta\tau_1}{(\tau^{T \rightarrow X})^2} - \frac{\Delta\tau_2}{(\tau^{X \rightarrow R})^2}. \end{aligned} \quad (\text{C14})$$

This characterizes the local sensitivity of ζ to motion-induced changes in the bistatic geometry, revealing an inverse-square dependence on the segment delays.

For a fixed Tx-Rx deployment, the target is confined to a bounded sensing region and cannot approach the transmitter or receiver arbitrarily closely. Therefore, there exists a strictly positive lower bound $\tau_{\min} > 0$ such that

$$\tau_{\min} \leq \tau^{T \rightarrow X}, \tau^{X \rightarrow R}. \quad (\text{C15})$$

Using this bound together with (C14), the variation of ζ can be upper-bounded as

$$|\Delta\zeta| \leq \frac{|\Delta\tau_1|}{(\tau^{T \rightarrow X})^2} + \frac{|\Delta\tau_2|}{(\tau^{X \rightarrow R})^2} \leq \frac{|\Delta\tau_1| + |\Delta\tau_2|}{\tau_{\min}^2}. \quad (\text{C16})$$

This bound shows that, as long as the target remains within the sensing region, the geometry-dependent factor ζ evolves slowly over time.

In contrast, the total bistatic propagation delay is given by the sum of the two segment delays, and its variation directly reflects the target-induced path-length changes:

$$\Delta(\tau^{T \rightarrow X} + \tau^{X \rightarrow R}) \approx \Delta\tau^{T \rightarrow X} + \Delta\tau^{X \rightarrow R}. \quad (\text{C17})$$

This indicates that the total bistatic delay varies on the same time scale as the target motion, whereas the geometry-dependent factor ζ is much less sensitive to such motion-induced variations.

Combining the observations from (C16) and (C17), the product

$$\tilde{\Gamma}^X \triangleq \zeta \Gamma^X \quad (\text{C18})$$

can be treated as a constant and obtained via a one-time calibration under the same operating conditions. Under this approximation, the NLOS path amplitude can be simplified as

$$\rho^X = \frac{\tilde{\Gamma}^X}{\tau^{T \rightarrow X} + \tau^{X \rightarrow R}}, \quad (\text{C19})$$

indicating that the dynamic-path amplitude is primarily governed by the total bistatic propagation delay.

References

- [1] Zhang, J.A., Liu, F., Masouros, C., Heath, R.W., Feng, Z., Zheng, L., Petropulu, A.: An overview of signal processing techniques for joint communication and radar sensing. *IEEE Journal of Selected Topics in Signal Processing* **15**(6), 1295–1315 (2021)
- [2] Liu, F., Masouros, C., Eldar, Y.C.: *Integrated Sensing and Communications*. Springer, Cham (2023)
- [3] Feng, Y., Xie, Y., Ganesan, D., Xiong, J.: Lte-based low-cost and low-power soil moisture sensing. In: *Proceedings of the 20th ACM Conference on Embedded Networked Sensor Systems*, pp. 421–434 (2022)

- [4] Wu, K., Wang, Z., Chen, S.-L., Zhang, J.A., Guo, Y.J.: Isac: From human to environmental sensing. arXiv preprint arXiv:2507.13766 (2025)
- [5] Wang, Z., Zhang, J.A., Wu, K., Guo, Y.J.: Water level sensing via communication signals in a bi-static system. arXiv preprint arXiv:2505.19539 (2025)
- [6] Masood, K.F., Wu, K., Wang, Z., Zhang, J.A., Chen, S.-L., Guo, Y.J.: Efficient river water level sensing using cellular csi and joint space-time processing. arXiv preprint arXiv:2509.01905 (2025)
- [7] Xu, Y., Wu, K., Zhang, J.A., Wang, Z., Jayawickrama, B.A., Guo, Y.J.: Smartphone-based experimental analysis of rainfall effects on lte signal indicators. *Sensors* **25**(2), 375 (2025)
- [8] Pegoraro, J., Lacruz, J.O., Azzino, T., Mezzavilla, M., Rossi, M., Widmer, J., Rangan, S.: Jump: Joint communication and sensing with unsynchronized transceivers made practical. *IEEE Transactions on Wireless Communications* **23**(8), 9759–9775 (2024)
- [9] Miao, F., Huang, Y., Lu, Z., Ohtsuki, T., Gui, G., Sari, H.: Wifi sensing techniques for human activity recognition: Brief survey, potential challenges, and research directions. *ACM Computing Surveys* **57**(5), 1–30 (2025)
- [10] Wang, Z., Zhang, J.A., Wu, K., Xu, M., Guo, Y.J.: Towards siso bistatic sensing for isac. arXiv preprint arXiv:2508.12614 (2025)
- [11] Feng, Y., Xie, Y., Ganesan, D., Xiong, J.: Lte-based pervasive sensing across indoor and outdoor. In: *Proceedings of the 19th ACM Conference on Embedded Networked Sensor Systems*, pp. 138–151 (2021)
- [12] Chen, C., Zhou, G., Lin, Y.: Cross-domain wifi sensing with channel state information: A survey. *ACM Computing Surveys* **55**(11), 1–37 (2023)
- [13] Du, R., Hua, H., Xie, H., Song, X., Lyu, Z., Hu, M., Xin, Y., McCann, S., Montemurro, M., Han, T.X., *et al.*: An overview on ieee 802.11 bf: Wlan sensing. *IEEE Communications Surveys & Tutorials* **27**(1), 184–217 (2024)
- [14] Yang, Z., Zhou, Z., Liu, Y.: From rss to csi: Indoor localization via channel response. *ACM Computing Surveys (CSUR)* **46**(2), 1–32 (2013)
- [15] Dubey, A., Sood, P., Santos, J., Ma, D., Chiu, C.-Y., Murch, R.: An enhanced approach to imaging the indoor environment using wifi rss measurements. *IEEE Transactions on Vehicular Technology* **70**(9), 8415–8430 (2021)
- [16] Rappaport, T.S.: Wireless communications–principles and practice, (the book end). *Microwave Journal* **45**(12), 128–129 (2002)
- [17] Srinivasa, S., Haenggi, M.: Path loss exponent estimation in large wireless networks. In: *2009 Information Theory and Applications Workshop*, pp. 124–129 (2009). IEEE
- [18] Yiu, S., Dashti, M., Claussen, H., Perez-Cruz, F.: Wireless rss fingerprinting localization. *Signal Processing* **131**, 235–244 (2017)
- [19] Chatzimichail, A., Tsanousa, A., Meditskos, G., Vrochidis, S., Kompatsiaris, I.: Rssi fingerprinting techniques for indoor localization datasets. In: *Interactive Mobile Communication, Technologies and Learning*, pp. 468–479. Springer, Cham (2019)
- [20] Wang, Y., Cheng, H., Meng, M.Q.-H.: A learning-based sequence-to-sequence wifi fingerprinting framework for accurate pedestrian indoor localization using unconstrained rss. *IEEE Internet of Things Journal* (99), 1–1 (2025)
- [21] Wu, K., Pegoraro, J., Meneghelli, F., Zhang, J.A., Lacruz, J.O., Widmer, J., Restuccia, F., Rossi, M., Huang, X., Zhang, D., Caire, G., Guo, Y.J.: Sensing in bistatic isac systems with clock asynchronism: A signal processing perspective. *IEEE Signal Processing Magazine* **41**(5), 31–43 (2024) <https://doi.org/10.1109/MSP.2024.3418725>

- [22] Qian, K., Wu, C., Zhang, Y., Zhang, G., Yang, Z., Liu, Y.: Widar2. 0: Passive human tracking with a single wifi link. In: ACM MobiSys, pp. 350–361 (2018)
- [23] Wang, Z., Zhang, J.A., Xu, M., Guo, J.: Single-target real-time passive wifi tracking. IEEE Transactions on Mobile Computing **2**(6), 3724–3742 (2023)
- [24] Wang, Z., Zhang, J.A., Zhang, H., Xu, M., Guo, J.: Passive human tracking with wifi point clouds. IEEE Internet of Things Journal **12**(5), 5528–5543 (2025) <https://doi.org/10.1109/JIOT.2024.3487193>
- [25] Chen, K., Zhang, J.A., Wang, Z., Guo, Y.J.: Development of an uplink sensing demonstrator for perceptive mobile networks. In: 2023 22nd International Symposium on Communications and Information Technologies (ISCIT), pp. 191–196 (2023). IEEE
- [26] Meneghelli, F., Garlisi, D., Fabbro, N.D., Tinnirello, I., Rossi, M.: Sharp:environment and person independent activity recognition with commodity ieee 802.11 access points. IEEE Transactions on Mobile Computing **22**(10), 6160–6175 (2023) <https://doi.org/10.1109/TMC.2022.3185681>
- [27] Hu, Y., Wu, K., Andrew Zhang, J., Deng, W., Jay Guo, Y.: Cross-frequency sensing in bistatic isac systems. IEEE Transactions on Wireless Communications, 1–1 (2025) <https://doi.org/10.1109/TWC.2025.3585944>
- [28] Tadayon, N., Rahman, M.T., Han, S., Valaee, S., Yu, W.: Decimeter ranging with channel state information. IEEE Transactions on Wireless Communications **18**(7), 3453–3468 (2019) <https://doi.org/10.1109/TWC.2019.2914194>
- [29] Halperin, D., Hu, W., Sheth, A., Wetherall, D.: Tool release: Gathering 802.11 n traces with channel state information. ACM SIGCOMM computer communication review **41**(1), 53–53 (2011)
- [30] Inc., T.I.: IWR1642 Evaluation Module (IWR1642BOOST) Single-Chip mmWave Sensing Solution User’s Guide. User’s Guide SWRU521C (May 2017). Texas Instruments Incorporated. Revised May 2020. <https://www.ti.com/lit/ug/swru521c/swru521c.pdf>